nanomaterials

MDPI

Article

Probing into the In-Situ Exsolution Mechanism of Metal Nanoparticles from Doped Ceria Host

Lifang Zhang [1], Weiwei Ji [1], Qiyang Guo [1], Yu Cheng [1,*], Xiaojuan Liu [2,3], Hongbin Lu [1,*] and Hong Dai [1,*]

[1] School of Chemistry and Chemical Engineering, Nantong University, Nantong 226009, China; lfzhang@ntu.edu.cn (L.Z.); 1808041069@stmail.ntu.edu.cn (W.J.); gyguo@ntu.edu.cn (Q.G.)
[2] State Key Laboratory of Rare Earth Resource Utilization, Changchun Institute of Applied Chemistry, Chinese Academy of Sciences, Changchun 130022, China; lxjuan@caic.ac.cn
[3] University of Science and Technology of China, Hefei 230026, China
* Correspondence: chengyu@ntu.edu.cn (Y.C.); luhb@nju.edu.cn (H.L.); dh123@ntu.edu.cn (H.D.)

Abstract: Exsolved nanoparticle catalysts have recently attracted broad research interest as they simultaneously combine the features of catalytic activity and chemical stability in various applications of energy conversion and storage. As the internal mechanism of in-situ exsolution is of prime significance for the optimization of its strategy, comprehensive research focused on the behaviors of in-situ segregation for metal (Mn, Fe, Co, Ni, Cu, Ag, Pt and Au)-substituted CeO_2 is reported using first-principles calculations. An interesting link between the behaviors of metal growth from the ceria host and their microelectronic reconfigurations was established to understand the inherent attribute of metal self-regeneration, where a stair-stepping charge difference served as the inner driving force existing along the exsolving pathway, and the weak metal-coordinate associations synergistically facilitate the ceria's in-situ growth. We hope that these new insights provide a microscopic insight into the physics of in-situ exsolution to gain a guideline for the design of nanoparticle socketed catalysts from bottom to top.

Keywords: in-situ exsolution mechanism; doped ceria; metal nanoparticle

Citation: Zhang, L.; Ji, W.; Guo, Q.; Cheng, Y.; Liu, X.; Lu, H.; Dai, H. Probing into the In-Situ Exsolution Mechanism of Metal Nanoparticles from Doped Ceria Host. *Nanomaterials* **2021**, *11*, 2114. https://doi.org/10.3390/nano11082114

Academic Editors: Frederik Tielens and Xianfu Wang

Received: 26 July 2021
Accepted: 18 August 2021
Published: 19 August 2021

1. Introduction

Metal nanoparticle-tailored surfaces with high catalytic active-site density exhibit excellent electrocatalytic and/or photocatalytic performances in energy storages and converters such as storage batteries, fuel cells and photocatalytic water splitting [1–5]. Many tremendous efforts, for example, the deposition techniques through chemical or physical methods, have been devoted to design and construct the metal nanoparticles distributing onto the surface as the active sites during the catalysis [6–8]. However, the nanocatalyst obtained from the conventional impregnation approaches often suffers not only the uncontrollability of nanoparticles (size, distribution ratio and anchor sites) during preparation, but also the instability of functional surface due to nanoparticles agglomeration in the working environment, especially for the high-temperature service such as the traditional solid oxide fuel cells (SOFCs) and solid oxide electrolysis cells (SOECs) [8,9]. Therefore, in-situ exsolution, in which nanoparticles directly grow from the parent material and strongly anchor at its surface by the applications of reduction, thermal treatment or electrochemical potential, has received rising attention [10–13].

Because of its facile process without expensive precursors and multiple "impregnation" steps, in-situ exsolution has become one of the promising, time- and cost-effective strategies to manufacture the controllable and stable nano-catalysts. Metal nanoparticles, such as precious metals (Ag, Pt, Au, etc.) or transition metals (Ni, Co, Cu, etc.), have been successfully exsolved from ABO_3-type perovskites [14–19]. Taking $LaFe_{1-x}M_xO_3$ (M represents the metals elements) as an example, the catalytically active metal ions M are used as the dopants assimilated into the B-site of parent material $LaFeO_3$, which would

subsequently in-situ socket onto the surface forming metal nanoparticles under the reducing atmosphere [20–22]. As compared to the traditional deposition techniques, the in-situ growth of nanoparticles "pinned" on the perovskite surfaces exhibit excellent electrochemical activities and exceptional stabilities in automotive emission catalysts, as well as the novel electrodes for SOFCs and SOECs [23–25]. According to a great deal of studies, it is largely accepted that there are two core requirements in an in-situ exsolution process: one is the solubility for these catalyst elements in parent-oxides under the oxidizing conditions, and another is that the formation energies of nanoparticle-decorated surface must be low enough for the catalyst elements' egress and anchorage [26–28]. Obviously, the influence factors contributing to the quality of in-situ exsolving nanoparticles are very complicated, which include surface orientation and composition, catalyst element, deficiency species, reductive condition and so on. For example, a previous article indicated that the expected Ni-nanoparticles were successfully formulated in the $La_{0.4}Sr_{0.4}Ti_{0.97}Ni_{0.03}O_{31-\delta}$ system as an increased concentration of surface La-ion [29]. Irvine group showed that the A-site deficiency in the $AB_{11-x}M_xO_{3-\delta}$ accelerates the in-situ growth of transition metal nanoparticles [30]. Recently, Gao et al. revealed that Ni preferentially segregates toward the 100-oriented and SrTiO-terminated surface with ab initio computations, which was consistent with previous experiments [31].

Over the last few decades, the most frequent studies for the in-situ growth phenomenon have focused on the material families of perovskite oxides. With the exception of the perovskite families, the strategy of in-situ exsolution branches out to the rutile, layered K_2NiF_4-type, fluorite-structured oxides, etc., which also possess favorable electrochemical performance as electrodes [32–35]. Boulfrad et al. applied the technique of in-situ exsolution to the rutile-type structure $NbTi_{0.5}Ni_{0.5}O_4$ (NTNO) and showed the potential of nano-scaled Ni particles decorated NTNO as a SOFC anode [36]. Sengodan et al. fabricated layered perovskite $PrBaMn_2O_{5+\delta}$ (PBMO) by in-situ annealing of $Pr_{0.5}Ba_{0.5}MnO_{3-\delta}$, which exhibited high electrical conductivity and remarkable redox stability as ceramic anode material for SOFC [37]. Moreover, Pilger et al. presented a possible segregation strategy for the fabrication of size controllable Pt particles on fluorite-structured ceria via an incorporation−segregation mechanism [38]. It was found that Pt/CeO_2 nanomaterial with the segregated Pt particles had a nature of remarkable activity and thermal stability as a catalyst in CO oxidation. However, up to now, a systematic regulation of in-situ growth is still unavailable for the exsolution phenomena, such as the external condition in the process of in-situ segregation, the inner driving force for nanoparticle emergence, as well as the identifiable characteristic of parent materials, especially from micro-perspective.

As is well-known, fluorite-structured CeO_2 is widely utilized in various catalytic processes not only as a support or additive, but also as an active phase of the reaction, particularly in a SOFC system, due to its excellent performance in intermediate/low-temperature conditions [39–41]. Implementing the strategy of in-situ exsolution to metal-doped ceria, their catalytic activity and thermal stability can be further improved as reported previously. For instance, more recently, Tan et al. demonstrated that Ni nanoparticles could be strongly attached to the surface of Ni:Gd co-doped CeO_2 (NGDC) by exsolution procedures [42]. The Ni exsolved NGDC as the anode functional layer revealed a great promotion on the electrochemical performance at the anode supported SOFC under the lower temperature condition. In principle, it is of vital importance to recognize the determining factors of nanoparticle growth, which could make it possible to precisely control the qualities of nanoparticles, so that enhancing the catalytic activity of nanocatalysts with a few strategy optimizations. Nevertheless, there is no in-depth understanding of metal exsolution from the ceria host, and the studies concerning their mechanism of in-situ exsolution are rarely reported.

Herein, taking CeO_2 as the parent material, we focus on the behaviors of in-situ segregation in $M_xCe_{1-x}O_2$ (M including transition metals: Mn, Fe, Co, Ni and Cu, and precious metals: Ag, Pt and Au) by using density functional theory (DFT) simulations, aiming to establish a comprehensive understanding about the strategy of in-situ exsolution.

In particular, the influencing factors—species of exsolved elements, three different orientation surfaces (001)-, (011)- and (111)-oriented, respectively, and their microstructures—are detailed investigated to find out the key determinant in the CeO_2 host system. More crucially, the relationship between in-situ exsolution behavior and electronic structures is systematically analyzed to illustrate the inner driving force of nanoparticle exsolution. The analyses of other influence factors, for example, oxygen vacancy, will be the subject of our future work.

Computational Details

All of our first-principles calculations were implemented in the Vienna ab-initio simulation package (VASP) with the projector-augmented wave (PAW) approach. The generalized gradient approximation (GGA) with the basic of the modified Perdew–Burke–Ernzerhof (PBE_sol) functional was exploited to describe the exchange–correlation interaction [43–46]. Fluorite-structured CeO_2 with lattice parameter (a) of 5.411 Å, in accordance with experiment obtained crystal structure [47], was severed as the basic structure to build the investigated models. The kinetic energy cutoff was chosen to be 450 eV. As shown in Figure 1, three kinds of slab models were simulated as the corresponding surface systems. All geometry optimizations were performed within some common criteria, in which ionic relaxation was looped until Hellmann–Feynman force of each atom smaller than 0.005 eV/Å and electronic self-consistent convergence was relaxed to 10^{-5} eV. The spin-polarized method was applied to simulate energetic and electronic structures of each slab model based on the Monkhorst–Pack scheme [48] of $7 \times 7 \times 7$ k-point grid for the 12-atom primitive cell and $3 \times 3 \times 1$ k-point grid for all surface structures with (100)-, (110)- and (111)-oriented. Additionally, the strong correlations inside the metal d electrons and Ce-4f electrons were taken into consideration by the correction of onsite Coulomb interaction U within the setting of $U_{eff@Ce}$ = 5.5 eV, $U_{eff@M}$ = 4.5 eV during all of the DFT simulations, which approximated the previous literature [40,49]. To explore their charge distribution, the Bader method was used to estimate the effective charges of each atom availably [50], and the visualization for electronic and structural analysis (VESTA) was utilized to visualize the charge density distribution both from two-dimensional and three-dimensional perspectives straightforwardly [51].

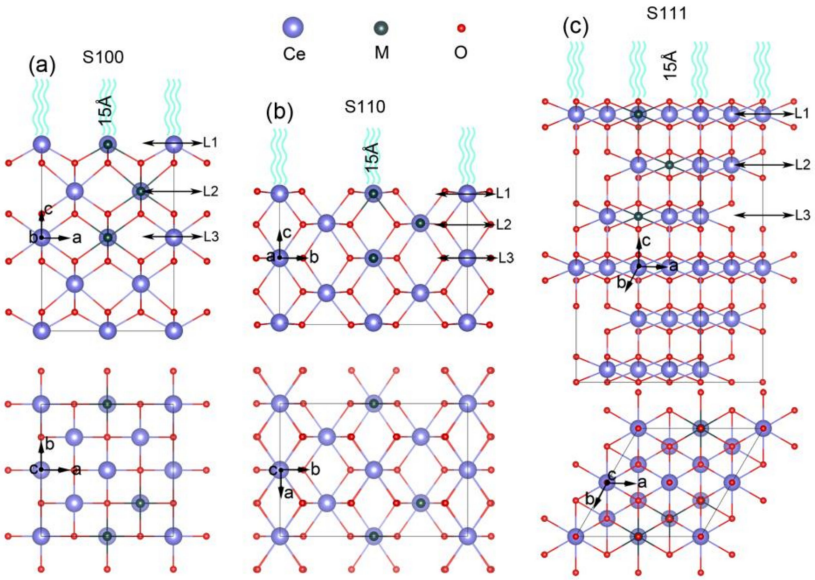

Figure 1. Side views (upper panel) and top views (lower panel) of modeled surfaces for $M_xCe_{1-x}O_2$. (**a**) 100-oriented slab labeled with S100, (**b**) 110-oriented slab labeled with S110 and (**c**) 111-oriented slab labeled with S111.

2. Results and Discussion

2.1. Construction of Metal Exsolved Surface Structures $M_xCe_{1-x}O_2$

To find out the factors of in-situ exsolution, taking the cubic-fluorite CeO_2 as the parent material [52], three types of slab models with different orientations were fabricated as the corresponding surface systems. From the side and top views, the (100)-oriented and (110)-oriented CeO_2 surfaces are comprised of five layers of Ce atoms with 2 Ce in each layer which is labeled by S100 and S110 as shown in Figure 1a,b, respectively. The (111)-oriented model is built of six layers of Ce atoms (Figure 1c) with the sixth layer of Ce and their coordinated O frozen according to previous study [53]. Moreover, each slab model contains a 15 Å vacuum layer which is as far away as possible to avoid interactions between the periodic slabs. As schemed in Figure 1, the upper three layers of all slabs (from the top down) are straightforwardly labeled with Layer 1 (L1 defined as the surface layer), Layer 2 (L2), and Layer 3 (L3 as the bulk layer). Because of their diverse expressions for different kinds of metal nanoparticles from the in-situ exsolution strategy, a series of metal atoms (M), including transition metal (Mn, Fe, Co, Ni and Cu) and precious metal (Ag, Pt, and Au), are taken into consideration to explore exsolution process in terms of element species [4,39]. Therefore, according to the previous literature, the Ce atom located at different layers was comparatively substituted with the M atom to simulate the process of nanoparticle segregation. Here, M substitution in L3 is defined as the solid-solution state, which means M is solved in the parent material, and M at L1 represents the surface segregated states to fabricate the nanoparticles anchored structures [27,31].

It is noticeable that surface stability is the prerequisite for the nanoparticle exsolution system, which can be evaluated by the DFT calculations of the surface formation energy (E_f^{surf}) given by the formula as following [54]:

$$E_f^{surf} = \frac{1}{2S}\left(E_{slab}^{M_xCe_{1-x}O_2} - nE_{bulk}^{CeO_2} - mE_M + mE_{Ce}\right) \quad (1)$$

where $E_{slab}^{M_xCe_{1-x}O_2}$ is the total energy of slab containing an M substitution $M_xCe_{1-x}O_2$, $E_{bulk}^{CeO_2}$ is the total energy of pristine CeO_2 as the bulk phase, E_{Ce} and E_M are the chemical potential of the bulk phase for Ce and substituted atom M. n is the stoichiometric coefficient which equals the size of the surface slab, m is the number of the substituted atom, S is the surface area (with the unit of $Å^2$). The evolutions of E_f^{surf} as a function of M substitutions are obtained as summarized in Figure 2a for the surface of S100, Figure 2b for S110 and Figure 2c for S111. As we know, the negative value of E_{surf} suggests that the surface sample is energetically favorable, while the positive value means the instability of the surface system. Therefore, the undecorated CeO_2 surfaces S100, S110 and S111 with the positive values of E_f^{surf} are identified as the energetically unfavorable samples, which are in the order of S100 > S110 > S111. Obviously, S100 without M substitution is the most unstable surface to a certain extent. It is widely accepted that Ce cations are cubically (8-fold) coordinated with high symmetry in pristine CeO_2, while in CeO_2 surface, the exposed terminals with the unfavorable configuration but without the charge neutralization may theoretically cause their thermodynamic instability.

As the previous studies stated, aliovalent doping in the bulk phase of CeO_2 would give rise to instability, forming an oxygen vacancy or other structural defects in the crystal structures finally [40,55]. However, in this surface research, it is found that all of the investigated M substitutions can stabilize the surfaces in reverse. The substituting process may cause the charge neutralization to balance the surface structure through the inducement of symmetry breaking. As shown in Figure 2, the negative values, closely related to the type of substituted atoms, indicate the potentiality of nanoparticle anchored surfaces. Generally, as a comprehensive comparison between S100, S110 and S111 indicated, the system of M substituted S100 is the most stable among the three types of surface orientations; S111 follows closely and S110 comes last, which seems opposite to the undecorated cases. Moreover, it should be noted that in the transition metal substituted systems, Mn, Fe, Co

Ni and Cu are favorably located at the ceria surfaces and their stability increases orderly from Mn to Cu. Meanwhile, for precious metal cases, the abilities of surface formation for Ag and Au cases are energetically similar and the Pt case falls behind slightly. Although the difference among the M-doped systems of S100, S110 and S111 is conspicuous, their evolution tendencies along with Mn → Fe → Co → Ni → Cu → Ag → Pt → Au seem to be consistent apparently. The result outlined above shows that Cu is the most favorable case to locate on the surface of S100, and the stability of the M-anchored surface is strongly affected by the surface orientation, as well as the variety of M substitution.

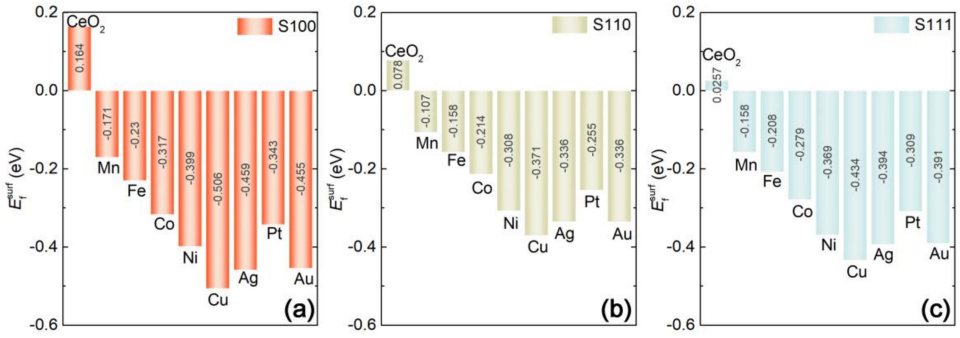

Figure 2. Surfaces formation energy (E_f^{surf}) of $M_xCe_{1-x}O_2$ slabs with different orientations: (**a**) for S100, (**b**) for S110 and (**c**) for S111.

From the viewpoint of surface stability, a brief hypothesis that the series of doped M can strongly bound to the surfaces of CeO_2 in the relevant orientations is given according to the investigation of surface energy, which is approximately consistent with the previous experiments [38,42,56]. However, it only proves the stability of M-substituted surface systems presumably attributed to the surface rearrangements with local distortions. There is no direct evidence to verify the feasibility of the process of M in-situ exsolution. Therefore, in the following, we directly estimate the surface segregation energy to study the energetics of the M self-regeneration process, and furtherly reveal the inner mechanism of in-situ exsolution, which has an association with the microscopic electronic configurations of surfaces.

2.2. Capabilities of In-Situ Exsolution in $M_xCe_{1-x}O_2$ Systems

As is well-known that it is hard to accurately observe the in-situ exsolution of experimental measurements. Taking the advantage of the DFT method which could fabricate some theoretical structures on the basis of idealized speculations, we first construct the series of $M_xCe_{1-x}O_2$ (see surface models in Figure 1a–c) to simulate the self-regeneration process of M from the ceria host. Figure 3a depicts a schematic diagram for the process of M segregation, possessing some similarities with the previous theoretical studies. As clarified above, the slab model with M substitution in L1 is regarded as the surface segregated state, and its energy is E^M_{surf}, while the slab with M in L3 is defined as the solid-solution state corresponding to the M in ceria bulk whose energy is E^M_{bulk}. Based on these definitions, we defined the energy difference between the system with M at L1 and the corresponding one with M in L3 as M segregation energy (E^M_{seg}) [27,31]:

$$E^M_{seg} = E^M_{surf} - E^M_{bulk} \quad (2)$$

It is widely accepted that E^M_{seg} is a direct energy-descriptor to probe into the feasibility of the M exsolution. As previous research suggested, when $E^M_{seg} > 0$, the doped M would be energetically stable in the bulk, while if $E^M_{seg} < 0$, M is preferably exsolved from the lattice to form an M nanoparticle protruded onto the surface. The calculation assessment of E^M_{seg} for each M substituted slab is summarized in Figure 3b, which shows the abilities of M to take part in the in-situ exsolution. Generally, all slab models expect for $Co_xCe_{1-x}O_2$-S110

case display $E_{seg}^{M} < 0$. With the comparison of E_{seg}^{M} between M-doped S100, S110 and S111, it is worth noting that S100 has the smallest E_{seg}^{M}. Obviously, the big differences of E_{seg}^{M} between these three surface systems indicate the strong orientation tendencies of the exsolution in the ceria host and M segregations are prone to anchor on S100, which is consistent with the speculation from the analysis of surface stabilities. In detail, each M substitution has its own orientation selection. Taking $Au_xCe_{1-x}O_2$ and $Co_xCe_{1-x}O_2$ cases as examples, the Au-doped case has the smallest $E_{seg}^{M} = -10.964$ eV in S100, while only -1.853 eV and -1.137 eV of E_{seg}^{M} for S110 and S111. The exsolution sequence for $Au_xCe_{1-x}O_2$ is S100 > S110 > S111, and most of the Au ingredient in the ceria host will selectively exsolve out to anchor on S100. For the $Co_xCe_{1-x}O_2$ case, there is also a lower negative value of E_{seg}^{M} for S100 ($E_{seg}^{M} = -7.079$ eV), and -1.638 eV of E_{seg}^{M} for S111. However, the positive value of E_{seg}^{M} (0.209) clearly points out that Co-nanoparticle is unfavored to exsolve out of the (110)-oriented surface. Co selectively segregates oriented in the order with S100 > S111 > S110. Moreover, we can also see that in the S100 system, all of the precious-metal-doped cases (Au, Pt, and Ag) and part of transition metals (Fe and Co) with comparatively low segregation energy of $E_{seg}^{M} < -5$ eV may lead to the acceleration for M exsolution. Thus, the potentialities of M exsolutions are arranged in rank order with Au > Pt > Ag for precious metals and Fe > Co > Cu > Mn > Ni for transition metals.

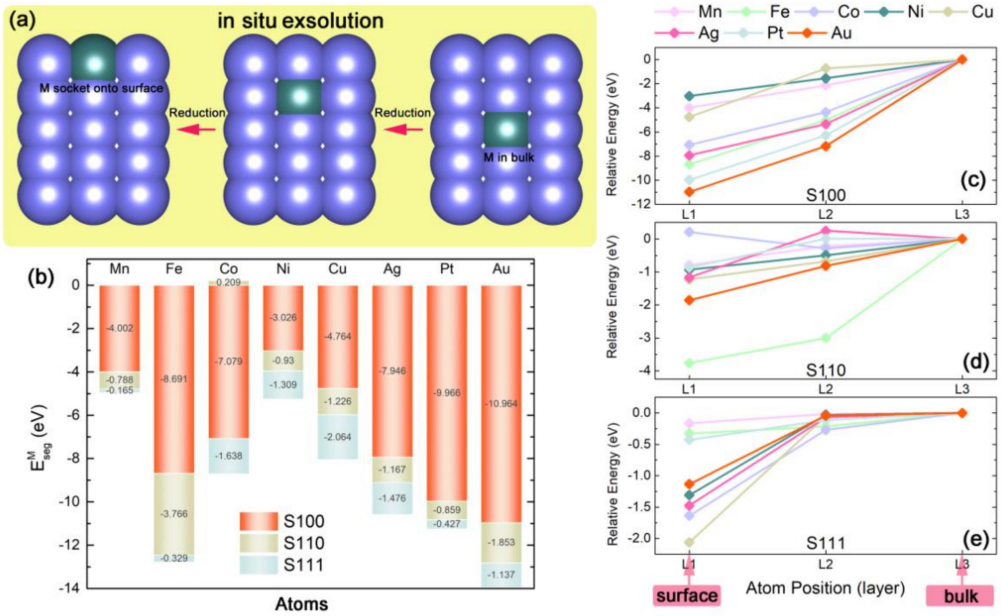

Figure 3. (**a**) The schematic diagram of metal M in-situ exsolution in term of atomic scale. (**b**) Evolution of the segregation energy E_{seg}^{M} for different oriented $M_xCe_{1-x}O_2$ slabs as a function of M substitutions. (**c**–**e**) Relative energy of $M_xCe_{1-x}O_2$ slabs of as a function of the position of metal atoms, (**c**) for S100, (**d**) for S110 and (**e**) for S111, the zero of energy is the energy of $M_xCe_{1-x}O_2$ slabs with M in the "bulk" as the reference basis.

Additionally, it was reported that the reductive condition of in-situ exsolution made a profound impact on the performance of nanoparticles, which may be relative to the energy barrier of self-regeneration. As schemed above, a "two-step" mechanism of M segregation is assumed in Figure 3a. The first step is M "activization", in which M rises up from L3 ("bulk") to L2, the next step is M "stabilization" for M grows up from L2 to L1 ("surface") [27]. Herein, the relative energy of each exsolution case, which is the energy of each individual $M_xCe_{1-x}O_2$ slab minus E_{bulk}^{M}, is also estimated to measure the process of M self-regeneration. The energy gap between each step is defined as the limiting energy barrier. Analyzed the variations of the relative energies between three orientation slabs as shown in Figure 3c–e, it can be found that the energy gaps among the two steps in the S100 system are distinct as a whole, which means the pathway of M exsolution along

the (100)-orientation is energetically unobstructed. Meanwhile, in the S111 system, even though $E_{seg}^{M} < 0$, the gaps are ill-defined at the second step, leading to an impediment for M growth in this step. Thus, from the viewpoint of evolved relative energy, a certain energy gap among each step is expected to play an important role in the efficiency of M self-regeneration.

The above results, taken together, show the segregation ability of each $M_xCe_{1-x}O_2$, both for transition metals and precious metals, and firstly propose that the related M-substitutions are extraordinarily favored to segregate toward the (100)-oriented surface of ceria host. It is inferred the property of M self-regeneration is closely related to certain local distortions because of the surface rearrangements. In this ceria host, structural distortion certainly has an influence on the M-emergence in some form. In Figure 4, the variations of M_n–O bond length (M_n means M in the nth layer) reflect the local structural deformations as the function of M substitutions. On the one hand, the $M_xCe_{1-x}O_2$-S100 system, which possesses a high degree of variation for the bond length of M_1–O (Figure 4a) and M_2-O (Figure 4b) and few changes of M_3-O (Figure 4c) along the M dopants, has comparatively lower segregation energies in M exsolutions. On the other hand, $M_xCe_{1-x}O_2$-S110 with small changes in the degree of M_n–O (Figure 4d–f) and $M_xCe_{1-x}O_2$-S111 with large variation extents of M_n–O (Figure 4g–i) is energetically inefficient in the in-situ growth of M nanoparticles. This means that the degree of local distortion induced by the M segregation is proposed as a key structural parameter on the description of the exsolution feasibility, which is ultimately correlated with the electronic reconstructions derived from the surface rearrangements. Therefore, to relate these above results to relevant microscopic structural reconstruction, we further inspect the electronic properties in the following.

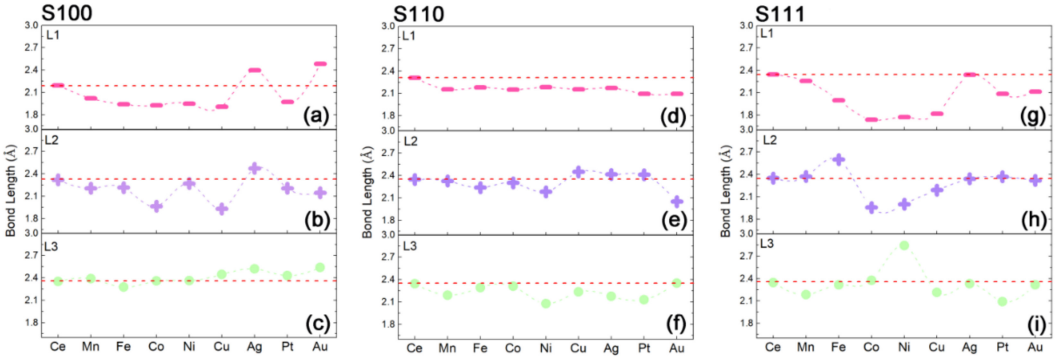

Figure 4. The evolution of M–O bond length as the function of M substitutions for each $M_xCe_{1-x}O_2$ slab: (**a**–**c**) for S100 system with M in L1 (**a**), L2 (**b**) and L3 (**c**), (**d**–**f**) for S110 system with M in L1 (**d**), L2 (**e**) and L3 (**f**), and (**g**–**i**) for S111 system with M in L1 (**g**), L2 (**h**) and L3 (**i**).

2.3. Intrinsic Mechanism of In-Situ Exsolution: Stair-Stepping Charge Difference

To investigate why the behavior of in-situ exsolution is quite different from the surface orientations, we firstly gain a deep insight into the charge density difference distribution of each oriented surface without M substitution, which are shown in Figure 5a (CeO_2-S100), Figure 5b (CeO_2-S110) and Figure 5c (CeO_2-S111). Here, flower-like electron clouds with blue color denote the positive electron density, and the negative electron density is expressed in yellow [57]. For the benefit of expression, the effective charges of relevant Ce-ions are indicated via Bader charge analysis obtained with DFT + U. See Figure 5a, it can be noted that the cloud shape of Ce_3 (with charge of +2.32e) and Ce_2 (+2.25e) looks like a "lotus", which hybridizes with O-2p adequately, while the low hybridization between the slender-shaped charge cloud of surface-Ce_1 (+1.54e) and O-2p contributes to the instability of surface [58]. Interestingly, a recognizable stair-stepping charge difference is found in CeO_2-S100, as the effective charge of Ce-ions declined from the bottom (L3) to the top (L1), which provides a facile way for M in-situ segregation. On the other hand, the plots of charge density difference for S110 (Figure 5b) and S111 (Figure 5c) show the high degree of bonding hybridization between Ce_n (Ce_3 2.36e, Ce_2 2.36e and Ce_1 2.27e for S110, Ce_3 2.38e,

Ce_2 2.43*e* and Ce_1 2.38*e* for S111) and corresponding O-2*p*. Their indistinct differences of effective charge may narrow the way of M exsolution. Consequently, it can be put forward that the charge distribution of initial configuration decisively determines the direction of in-situ exsolution, and a stair-stepping charge difference as the inner driving force found in CeO_2-S100 is beneficial to the M self-regeneration, which is in accordance with the exsolution orientation as calculated above.

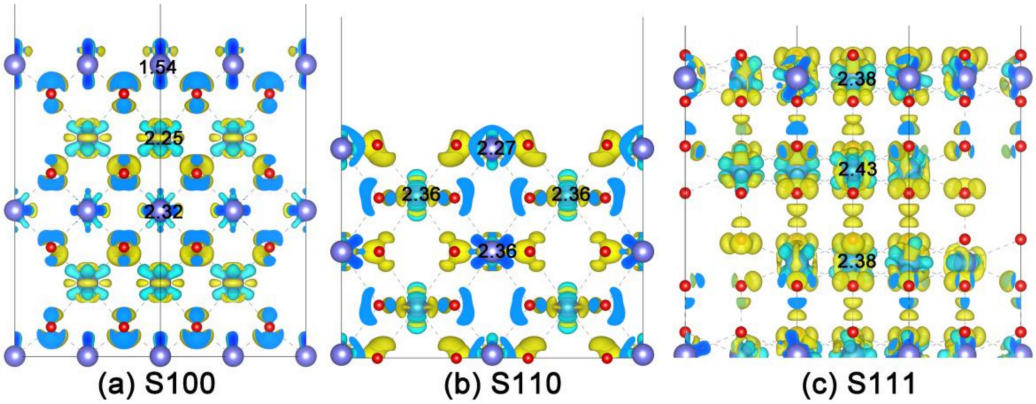

Figure 5. The 3D plots of charge density difference with an isosurface value of 0.02 e/Bohr^3 for pristine CeO_2 with different oriented surfaces: (**a**) for S100, (**b**) for S110 and (**c**) for S111.

Considering the M-doping effect on the potentiality of in-situ exsolution, we also analyze the charge density distribution and effective Bader charge of each M-ion for M-substituted cases. The 3D plots of charge density differences (taking $Pt_xCe_{1-x}O_2$ as an example) are shown in Figure 6a (for $Pt_xCe_{1-x}O_2$-S100), Figure S1 (for $Pt_xCe_{1-x}O_2$-S110) and Figure S2 ($Pt_xCe_{1-x}O_2$-S111), where the dopants (M-ions) including Ce are defined as M_3 to M_1 along the pathway of exsolution. For more details, we take $Fe_xCe_{1-x}O_2$ as the transition metal example (Figure S3). The remarkable changes of charge density distribution are demonstrated due to the surface rearrangement by M doping. It is clear that a certain degree of electron reconstructions emerges when M steps into the ceria host, which on the one hand compensates for the stabilities of surface slabs with the energy decreasing, and on the other hand bares some low-valent sites with high catalytic activity, especially in the $M_xCe_{1-x}O_2$-S100 case. Meanwhile, Figure 6b–d, Figure S1b–d and Figure S2b–d summarize the charge evolutions of metals (from M_1 to M_3) for $M_xCe_{1-x}O_2$-S100, $M_xCe_{1-x}O_2$-S110 and $M_xCe_{1-x}O_2$-S111, respectively. It is widely accepted that the low effective charges of metal ions manifest a comparatively weak association with surrounding coordination ions [59]. Here, we can see that the changes in the degree of effective charge reduction for $M_{1/2/3}$ in each layer as a function of M substitutions are approximately consistent with the order of M segregation obtained above. For instance, also taking $Pt_xCe_{1-x}O_2$-S100 as the example, the weaker bonding of $Pt_{1/2/3}$-O in $Pt_xCe_{1-x}O_2$-S100 because of the low charged Pt-ions leads to a better capability of exsolution. Hence, based on the detailed analysis of Bader charge [60], another determining parameter, the bonding strength between $M_{1/2/3}$-O, is proposed as the second significant factor for in-situ exsolution.

Moreover, for more intuitive information, the sectional drawings of charge density difference along the (001)-direction as shown in Figure 7a and Figure S4a ($M_xCe_{1-x}O_2$-S100 with Pt/Fe on "surface"), and Figure 7b and Figure S4b ($M_xCe_{1-x}O_2$-S100 with Pt/Fe in L2) and Figure 7c and Figure S4c ($M_xCe_{1-x}O_2$-S100 with Pt/Fe in "bulk"), are extracted to unmask the process of in-situ exsolution. In Figure 7c, when Pt is in L3, a characteristic electric potential difference exists along the pathway of Pt migration, which provides an inner drive-force to set the stage for Pt exsolution. When Pt is in L2, as shown in Figure 7b, it is worth noting the Pt-coordinate association—the connection between Pt_2 and their coordination O ions is rather weak. This infirm association facilitates the Pt's "escape" from

L2 to the surface. Ultimately, the exsolved Pt with the dumbbell-shaped electron cloud (as plotted in Figure 7a) is well anchored on the ceria surface, causing the nano-socketed structure to simultaneously possess surface stability and catalytic activity. To sum up, a reasonable exsolution mechanism for the $M_xCe_{1-x}O_2$ surface is proposed in our theoretical study.

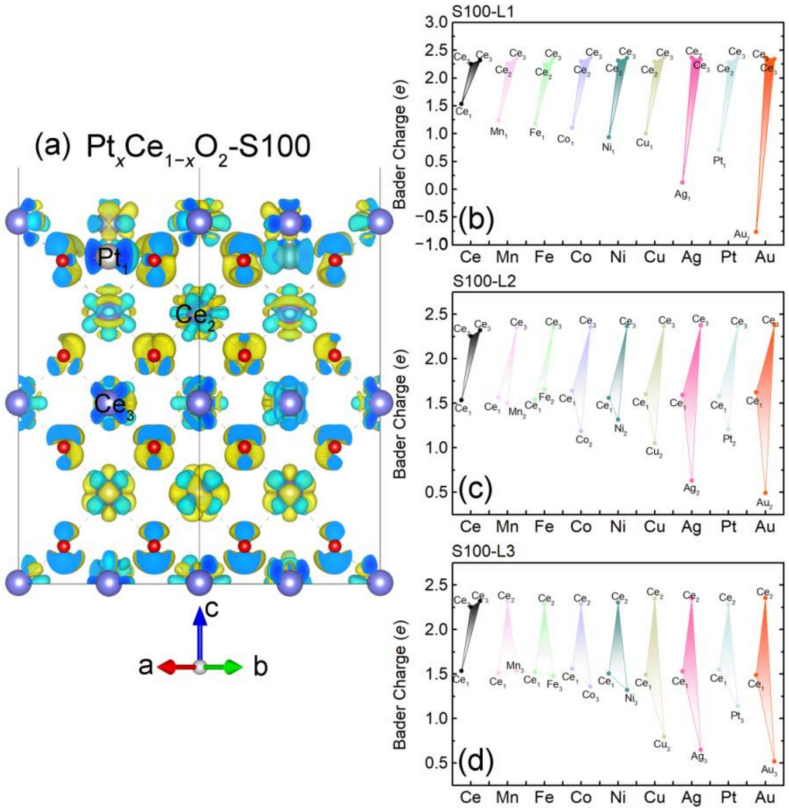

Figure 6. (**a**) The 3D plot of charge density difference with an isosurface value of 0.02 e/Bohr^3 for $Pt_xCe_{1-x}O_2$-S100 with Pt at L1. (**b**–**d**) Evolution of Bader charge for $M_xCe_{1-x}O_2$-S100 with the dependence of Mn, Fe, Co, Ni, Cu, Ag, Pt and Au: (**b**) M in L1, (**c**) M in L2 and (**d**) M in L3, the relevant M site are labeled as M_1, M_2 and M_3.

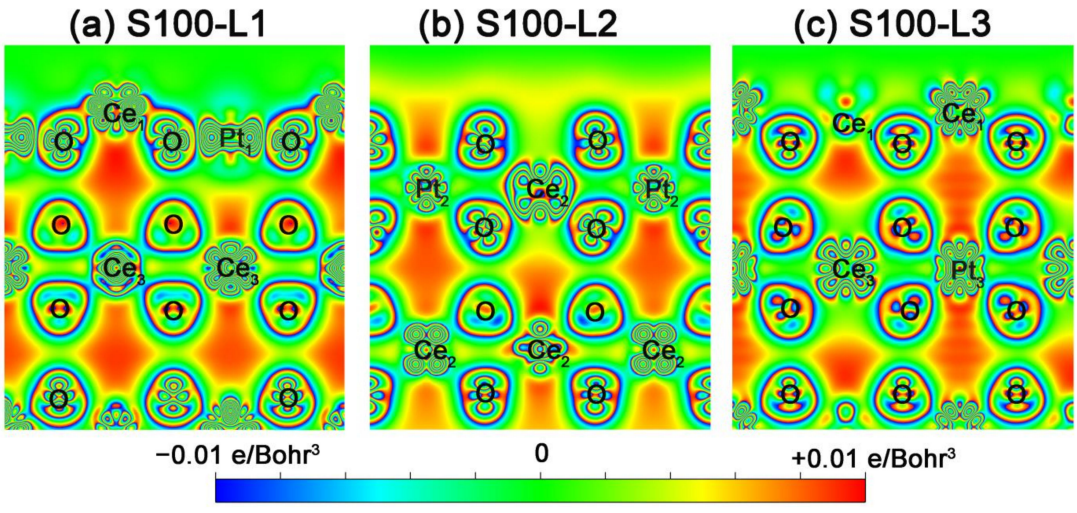

Figure 7. 2-D charge density difference plots along the (001)-direction (Δn (**r**) in units of e/Bohr^3) for 1.5 × 1.5 × 1 $Pt_xCe_{1-x}O_2$-S100, which with Pt (**a**) on surface layer L1, (**b**) in second layer L2 and (**c**) in the "bulk" layer L3.

3. Conclusions

In summary, we theoretically investigate the process of in-situ exsolution for ceria-based fluorite framework $M_xCe_{1-x}O_2$ (Mn, Fe, Co, Ni, Cu, Ag, Pt and Au). Our calculations of surface formation energy and M segregation energy show that the substituted M preferentially toward the (100)-oriented ceria surfaces and their stabilities and exsolution actives are sensitive to the dopant species M. It is found that Au/Pt/Ag/Fe/Co-doped S100 with smaller segregation energy can energetically accelerate the M self-regeneration, while the exsolution process in Cu/Ni/Mn-doped S100 may need more harsh reduction conditions to urge the M's ascent. In particular, linking the potentiality of M segregation with their microelectronic structure, our study proposes two crucial synergistic factors to uncover the mechanism for the in-situ exsolution of M-doped ceria: one is the inner driving force, a stair-stepping charge difference existing along the pathway of M migration is considered as the prerequisite factor for M exsolution; another factor is served as "motion plus", the bonding strength between $M_{1/2/3}$-O, where it is believed that the weak M-coordinate association will accelerate the M's segregation. As a result, our new insights give a fundamental guideline for the design of the exsolved nanocatalysts, which is a step toward a reasonable understanding of the in-situ growth mechanism.

Supplementary Materials: The following are available online at https://www.mdpi.com/article/10.3390/nano11082114/s1, Figure S1: Electronic structure detail of $M_xCe_{1-x}O_2$-S110, Figure S2: Electronic structure detail of $M_xCe_{1-x}O_2$-S110, Figure S3: The 3D plots of charge density difference for $Fe_xCe_{1-x}O_2$ with different oriented surfaces, Figure S4: 2-D charge density difference plots for $Fe_xCe_{1-x}O_2$-S100.

Author Contributions: Formal analysis, W.J. and Q.G.; Funding acquisition, H.L.; Investigation, L.Z.; Software, X.L.; Supervision, H.D.; Writing—original draft, L.Z.; Writing—review & editing, Y.C. and H.L. All authors have read and agreed to the published version of the manuscript.

Funding: This research was funded by the National Natural Science Foundation of China, grant number 22072068.

Data Availability Statement: The data used to support the findings of this study are available subject to approval from the relevant departments through the corresponding author upon request.

Acknowledgments: Generous computing time supported by NanTong Key Laboratory of High Performance Computing (CP120130001) is gratefully acknowledged.

Conflicts of Interest: The authors declare no conflict of interest.

References

1. Nishihata, Y.; Mizuki, J.I.; Akao, T.; Tanaka, H.; Uenishi, M.; Kimura, M.; Okamoto, T.; Hamada, N. Self-Regeneration of a Pd-Perovskite Catalyst for Automotive Emissions Control. *Nature* **2002**, *418*, 164–167. [CrossRef]
2. Arico, A.S.; Bruce, P.; Scrosati, B.; Tarascon, J.M.; Van Schalkwijk, W. Nanostructured Materials for Advanced Energy Con-version and Storage Devices. *Nat. Mater.* **2005**, *4*, 366–377. [CrossRef] [PubMed]
3. Liu, S.; Wang, M.; Ji, H.; Shen, X.; Yan, C.; Qian, T. Altering the Rate-Determining Step over Cobalt Single Clusters Leading to Highly Efficient Ammonia Synthesis. *Natl. Sci. Rev.* **2020**, *8*. [CrossRef]
4. Ding, W.-L.; Cao, Y.-H.; Liu, H.; Wang, A.-X.; Zhang, C.-J.; Zheng, X.-R. In Situ Growth of NiSe@$Co_{0.85}$Se Heterointerface Structure with Electronic Modulation on Nickel Foam for Overall Water Splitting. *Rare Met.* **2020**, *40*, 1373–1382. [CrossRef]
5. Xia, Z.; Liu, G.; Wen, J.; Mei, Z.; Balasubramanian, M.; Molokeev, M.S.; Peng, L.; Gu, L.; Miller, D.J.; Liu, Q.; et al. Tuning of Photoluminescence by Cation Nanosegregation in the $(CaMg)_x(NaSc)_{(1-x)}Si_2O_6$ Solid Solution. *J. Am. Chem. Soc.* **2016**, *138*, 1158–1161. [CrossRef] [PubMed]
6. Niu, C.; Liu, J.; Qian, T.; Shen, X.; Zhou, J.; Yan, C. Single Lithiumion Channel Polymer Binder for Stabilizing Sulfur Cathodes. *Natl. Sci. Rev.* **2020**, *7*, 315–323. [CrossRef]
7. Dai, L.; Lu, X.; Chu, G.; He, C.; Zhan, W.; Zhou, G. Surface Tuning of $LaCoO_3$ Perovskite by Acid Etching to Enhance its Cat-alytic Performance. *Rere Met.* **2011**, *40*, 555–562. [CrossRef]
8. Kim, K.J.; Han, H.; Defferriere, T.; Yoon, D.; Na, S.; Kim, S.J.; Dayaghi, A.M.; Son, J.; Oh, T.S.; Jang, H.M.; et al. Facet-Dependent in Situ Growth of Nanoparticles in Epitaxial Thin Films: The Role of Interfacial Energy. *J. Am. Chem. Soc.* **2019**, *141*, 7509–7517. [CrossRef] [PubMed]

9. Zhu, Y.; Zhou, W.; Ran, R.; Chen, Y.; Shao, Z.; Liu, M. Promotion of Oxygen Reduction by Exsolved Silver Nanoparticles on a Perovskite Scaffold for Low-Temperature Solid Oxide Fuel Cells. *Nano Lett.* **2015**, *16*, 512–518. [CrossRef]
10. Tsekouras, G.; Neagu, D.; Irvine, J.T.S. Step-Change in High Temperature Steam Electrolysis Performance of Perovskite Oxide Cathodes with Exsolution of B-Site Dopants. *Energy Environ. Sci.* **2013**, *6*, 256–266. [CrossRef]
11. Zhang, X.; Zhang, W.; Zhang, L.; Meng, J.; Meng, F.; Liu, X.; Meng, J. Enhanced Electrochemical Property of $La_{0.6}Sr_{0.4}Co_{0.8}Fe_{0.2}O_3$ as Cathode for Solid Oxide Fuel Cell by Efficient In Situ Polarization-Exsolution Treatment. *Electrochim. Acta* **2017**, *258*, 1096–1105. [CrossRef]
12. Zhou, G.-F.; Ma, J.; Bai, S.; Wang, L.; Guo, Y. CO Catalytic Oxidation over Pd/CeO_2 with Different Chemical States of Pd. *Rare Met.* **2019**, *39*, 800–805. [CrossRef]
13. Sun, Y.; Zhang, Y.; Chen, J.; Li, J.-H.; Zhu, Y.-T.; Zeng, Y.-M.; Amirkhiz, B.S.; Hua, B.; Luo, J.-L. New Opportunity for in Situ Exsolution of Metallic Nanoparticles on Perovskite Parent. *Nano Lett.* **2016**, *16*, 5303–5309. [CrossRef]
14. Namba, K.; Ogura, S.; Ohno, S.; Di, W.; Kato, K.; Wilde, M.; Pletikosić, I.; Pervan, P.; Milun, M.; Fukutani, K. Acceleration of Hydrogen Absorption by Palladium through Surface Alloying with Gold. *Proc. Natl. Acad. Sci. USA* **2018**, *115*, 7896–7900. [CrossRef]
15. Zhang, Y.; Tao, H.-B.; Liu, J.; Sun, Y.; Chen, J.; Hua, B.; Thundat, T.; Luo, J.-L. A Rational Design for Enhanced Oxygen Reduction: Strongly Coupled Silver Nanoparticles and Engineered Perovskite Nanofibers. *Nano Energy* **2017**, *38*, 392–400. [CrossRef]
16. Xu, S.; Dong, D.; Wang, Y.; Doherty, W.; Xie, K.; Wu, Y. Perovskite Chromates Cathode with Resolved and Anchored Nickel Nano-Particles for Direct High-Temperature Steam Electrolysis. *J. Power Sour.* **2014**, *246*, 346–355. [CrossRef]
17. Kwon, O.; Sengodan, S.; Kim, K.; Kim, G.; Jeong, H.Y.; Shin, J.; Ju, Y.-W.; Han, J.W.; Kim, G. Exsolution Trends and Co-Segregation Aspects of Self-Grown Catalyst Nanoparticles in Perovskites. *Nat. Commun.* **2017**, *8*, 15967. [CrossRef] [PubMed]
18. Jiang, S.P. Nanoscale and Nano-Structured Electrodes of Solid Oxide Fuel Cells by Infiltration: Advances and Challenges. *Int. J. Hydrog. Energ.* **2012**, *37*, 449–470. [CrossRef]
19. Burnat, D.; Kontic, R.; Holzer, L.; Steiger, P.; Ferri, D.; Heel, A. Smart Material Concept: Reversible Microstructural Self-Regeneration for Catalytic Applications. *J. Mater. Chem. A* **2016**, *4*, 11939–11948. [CrossRef]
20. Tanaka, H.; Uenishi, M.; Taniguchi, M.; Tan, I.; Narita, K.; Kimura, M.; Kaneko, K.; Nishihata, Y.; Mizuki, J. Intelligent Catalyst having the Self-Regenerative Function of Pd, Rh and Pt for Automotive Emissions Control. *Catal. Today* **2006**, *117*, 321–328. [CrossRef]
21. Uenishi, M.; Tanaka, H.; Taniguchi, M.; Tan, I.; Nishihata, Y.; Mizuki, J.; Kobayashi, T. Time Evolution of Palladium Structure change with Redox Fluctuations in a LaFePdO3 Perovskite Automotive Catalyst by High-Speed Analysis with In Situ DXAFS. *Catal. Commun.* **2008**, *9*, 311–314. [CrossRef]
22. Hong, W.T.; Risch, M.; Stoerzinger, K.A.; Grimaud, A.; Suntivich, J.; Shao-Horn, Y. Toward the Rational Design of Non-Precious Transition Metal Oxides for Oxygen Electrocatalysis. *Energy Environ. Sci.* **2015**, *8*, 1404–1427. [CrossRef]
23. Götsch, T.; Schlicker, L.; Bekheet, M.F.; Doran, A.; Grünbacher, M.; Praty, C.; Tada, M.; Matsui, H.; Ishiguro, N.; Gurlo, A.; et al. Structural Investigations of $La_{0.6}Sr_{0.4}FeO_{3-\delta}$ under Reducing Conditions: Kinetic and Thermodynamic Limitations for Phase Transformations and Iron Exsolution Phenomena. *RSC Adv.* **2018**, *8*, 3120–3131. [CrossRef]
24. Tian, S.; You, W.; Shen, Y.; Gu, X.; Ge, M.; Ahmadi, S.; Ahmad, S.; Kraatz, H.B. Facile Synthesis of Silver-rich Au/Ag Bimetallic Nanoparticles with Highly Active SERS Properties. *New J. Chem.* **2019**, *43*, 14772–14780. [CrossRef]
25. Neagu, D.; Papaioannou, E.I.; Ramli, W.K.W.; Miller, D.N.; Murdoch, B.J.; Menard, H.; Umar, A.; Barlow, A.J.; Cumpson, P.J.; Irvine, J.T.S.; et al. Demonstration of Chemistry at a Point through Restructuring and Catalytic Activation at an-Chored Nanoparticles. *Nat. Commun.* **2017**, *8*, 1855. [CrossRef]
26. Sengodan, S.; Yeo, H.J.; Shin, J.Y.; Kim, G. Assessment of Perovskite-Type $La_{0.8}Sr_{0.2}Sc_xMn_{1-x}O_3$-Delta Oxides as Anodes for in-Termediate-Temperature Solid Oxide Fuel Cells Using Hydrocarbon Fuels. *J. Power Sour.* **2011**, *196*, 3083–3088. [CrossRef]
27. Hamada, I.; Uozumi, A.; Morikawa, Y.; Yanase, A.; Katayama-Yoshida, H. A Density Functional Theory Study of Self-Regenerating Catalysts $LaFe_{(1-x)}M_{(x)}O_{(3-y)}$ (M = Pd, Rh, Pt). *J. Am. Chem. Soc.* **2011**, *133*, 18506–18509. [CrossRef]
28. Li, B.; Katz, M.B.; Zhang, Q.; Chen, L.; Graham, G.W.; Pan, X. Surface-Termination-Dependent Pd Bonding and Aggregation of Nanoparticles on $LaFeO_3$ (001). *J. Chem. Phys.* **2013**, *138*, 144705. [CrossRef]
29. Neagu, D.; Oh, T.-S.; Miller, D.N.; Ménard, H.; Bukhari, S.M.; Gamble, S.R.; Gorte, R.J.; Vohs, J.M.; Irvine, J.T.S. Nano-Socketed Nickel Particles with Enhanced Coking Resistance Grown In Situ by Redox Exsolution. *Nat. Commun.* **2015**, *6*, 8120. [CrossRef]
30. Neagu, D.; Tsekouras, G.; Miller, D.N.; Ménard, H.; Irvine, J. In Situ Growth of Nanoparticles through Control of Non-Stoichiometry. *Nat. Chem.* **2013**, *5*, 916–923. [CrossRef]
31. Gao, Y.; Lu, Z.; You, T.L.; Wang, J.; Xie, L.; He, J.; Ciucci, F. Energetics of Nanoparticle Exsolution from Perovskite Oxides. *J. Phys. Chem. Lett.* **2018**, *9*, 3772–3778. [CrossRef] [PubMed]
32. Jacobson, A.J. Materials for Solid Oxide Fuel Cells. *Chem. Mater.* **2009**, *22*, 660–674. [CrossRef]
33. Liu, L.; Liu, R.; Xu, T.; Zhang, Q.; Tan, Y.; Zhang, Q.; Ding, J.; Tang, Y. Enhanced Catalytic Oxidation of Chlorobenzene over MnO_2 Grafted In Situ by Rare Earth Oxide: Surface Doping Induces Lattice Oxygen Activation. *Inorg. Chem.* **2020**, *59*, 14407–14414. [CrossRef] [PubMed]
34. Bera, P.; Patil, K.; Jayaram, V.; Subbanna, G.; Hegde, M. Ionic Dispersion of Pt and Pd on CeO_2 by Combustion Method: Effect of Metal–Ceria Interaction on Catalytic Activities for NO Reduction and CO and Hydrocarbon Oxidation. *J. Catal.* **2000**, *196*, 293–301. [CrossRef]

35. Gui, L.; Pan, G.; Ma, X.; You, M.; He, B.; Yang, Z.; Sun, J.; Zhou, W.; Xu, J.; Zhao, L. In-Situ Exsolution of CoNi Alloy Nanoparticles on $LiFe_{0.8}Co_{0.1}Ni_{0.1}O_2$ Parent: New opportunity for Boosting Oxygen Evolution and Reduction Reaction. *Appl. Surf. Sci.* **2020**, *543*, 148817. [CrossRef]
36. Boulfrad, S.; Cassidy, M.; Irvine, J.T. $NbTi_{0.5}Ni_{0.5}O_4$ as Anode Compound Material for SOFCs. *Solid State Ionics* **2011**, *197*, 37–41. [CrossRef]
37. Sengodan, S.; Ju, Y.W.; Kwon, O.; Jun, A.; Jeong, H.Y.; Ishihara, T.; Shin, J.; Kim, G. Self-Decorated MnO Nanoparticles on Double Perovskite Solid Oxide Fuel Cell Anode by in Situ Exsolution. *ACS Sustain. Chem. Eng.* **2017**, *5*, 9207–9213. [CrossRef]
38. Pilger, F.; Testino, A.; Carino, A.; Proff, C.; Kampolis, A.; Cervellino, A.; Ludwig, C. Size Control of Pt Clusters on CeO_2 Nanoparticles via an Incorporation–Segregation Mechanism and Study of Segregation Kinetics. *ACS Catal.* **2016**, *6*, 3688–3699. [CrossRef]
39. Wachsman, E.D.; Lee, K.T. Lowering the Temperature of Solid Oxide Fuel Cells. *Science* **2011**, *334*, 935–939. [CrossRef] [PubMed]
40. Zhang, L.; Meng, J.; Yao, F.; Zhang, W.; Liu, X.; Meng, J.; Zhang, H. Insight into the Mechanism of the Ionic Conductivity for Ln-Doped Ceria (Ln = La, Pr, Nd, Pm, Sm, Gd, Tb, Dy, Ho, Er, and Tm) through First-Principles Calculation. *Inorg. Chem.* **2018**, *57*, 12690–12696. [CrossRef] [PubMed]
41. Chen, Z.; Cao, F.-X.; Gao, W.; Dong, Q.-C.; Qu, Y.-Q. Uniform Small Metal Nanoparticles Anchored on CeO_2 Nanorods Driven by Electroless Chemical Deposition. *Rare Met.* **2019**, *39*, 806–814. [CrossRef]
42. Tan, J.; Lee, D.; Ahn, J.; Kim, B.; Kim, J.; Moon, J. Thermally Driven In-Situ Exsolution of Ni Nanoparticles from (Ni, Gd)CeO_2 for High-Performance Solid Oxide Fuel Cells. *J. Mater. Chem. A.* **2018**, *6*, 18133–18142. [CrossRef]
43. Kresse, G.; Furthmüller, J. Efficiency of Ab-Initio Total Energy Calculations for Metals and Semiconductors Using a Plane-Wave Basis Set. *Comput. Mater. Sci.* **1996**, *6*, 15–50. [CrossRef]
44. Kresse, G.; Furthmuller, J. Efficient Iterative Schemes for Ab Initio Total-Energy Calculations Using a Plane-Wave Basis Set. *Phys. Rev. B* **1996**, *54*, 11169–11186. [CrossRef]
45. Perdew, J.P.; Burke, K.; Ernzerhof, M. Generalized Gradient Approximation Made Simple. *Phys. Rev. Lett.* **1996**, *77*, 3865–3868. [CrossRef]
46. Perdew, J.P.; Ruzsinszky, A.; Csonka, G.I.; Vydrov, O.A.; Scuseria, G.E.; Constantin, L.; Zhou, X.; Burke, K. Restoring the Density-Gradient Expansion for Exchange in Solids and Surfaces. *Phys. Rev. Lett.* **2008**, *100*, 136406. [CrossRef]
47. Petit, L.; Svane, A.; Szotek, Z.; Temmerman, W.M. First-Principles Study of Rare-Earth Oxides. *Phys. Rev. B* **2005**, *72*, 205118. [CrossRef]
48. Monkhorst, H.J.; Pack, J.D. Special Ponits for Brillouin-Zone Integrations. *Phys. Rev. B* **1976**, *13*, 5188–5192. [CrossRef]
49. Pourovskii, L.; Amadon, B.; Biermann, S.; Georges, A. Self-Consistency over the Charge Density in Dynamical Mean-Field Theory: A Linear Muffintin Implementation and Some Physical Implications. *Phys. Rev. B* **2007**, *76*. [CrossRef]
50. Sanville, E.; Kenny, S.; Smith, R.; Henkelman, G. Improved Grid-Based Algorithm for Bader Charge Allocation. *J. Comput. Chem.* **2007**, *28*, 899–908. [CrossRef] [PubMed]
51. Momma, K.; Izumi, F. VESTA3 for Three-Dimensional Visualization of Crystal, Volumetric and Morphology Data. *J. Appl. Crystallogr.* **2011**, *44*, 1272–1276. [CrossRef]
52. Gerward, L.; Olsen, J.S.; Petit, L.; Vaitheeswaran, G.; Kanchana, V.; Svane, A. Bulk Modulus of CeO_2 and PrO_2-An Experimental and Theoretical Study. *J. Alloys Compd.* **2005**, *400*, 56–61. [CrossRef]
53. Anglès, X.A.; Roldan, A.; De Leeuw, N.H. Gadolinium-Vacancy Clusters in the (111) Surface of Gadolinium-Doped Ceria: A Density Functional Theory Study. *Chem. Mater.* **2015**, *27*, 7910–7917. [CrossRef]
54. Ma, H.; Chen, X.-Q.; Li, R.; Wang, S.; Dong, J.; Ke, W. First-Principles Modeling of Anisotropic Anodic Dissolution of Metals and Alloys in Corrosive Environments. *Acta Mater.* **2017**, *130*, 137–146. [CrossRef]
55. Andersson, D.A.; Simak, S.I.; Skorodumova, N.V.; Abrikosov, I.A.; Johansson, B. Optimization of Ionic Conductivity in Doped Ceria. *Proc. Natl. Acad. Sci. USA* **2006**, *103*, 3518–3521. [CrossRef] [PubMed]
56. Padi, S.P.; Shelly, L.; Komarala, E.P.; Schweke, D.; Hayun, S.; Rosen, B.A. Coke-Free Methane Dry Reforming over Nano-Sized NiO-CeO_2 Solid Solution after Exsolution. *Catal. Commun.* **2020**, *138*, 105951. [CrossRef]
57. Akbay, T.; Staykov, A.; Druce, J.; Tellez, H.; Ishihara, T.; Kilner, J.A. The Interaction of Molecular Oxygen on LaO Terminated Surfaces of La_2NiO_4. *J. Mater. Chem. A* **2016**, *4*, 13113–13124. [CrossRef]
58. Wang, Z.; Yang, W.; Zhu, Z.; Peng, R.; Wu, X.; Xia, C.; Lu, Y. First-Principles Study of O_2 Reduction on $BaZr_{1-x}Co_xO_3$ Cathodes in Protonic-Solid Oxide Fuel Cells. *J. Mater. Chem. A* **2014**, *2*, 16707–16714. [CrossRef]
59. Li, X.; Benedek, N.A. Enhancement of Ionic Transport in Complex Oxides through Soft Lattice Modes and Epitaxial Strain. *Chem. Mater.* **2015**, *27*, 2647–2652. [CrossRef]
60. Tang, W.; Sanville, E.; Henkelman, G. A Grid-Based Bader Analysis Algorithm without Lattice Bias. *J. Phys. Condens. Matter* **2009**, *21*, 084204. [CrossRef]